

XMM–Newton observations of the Galactic Centre Region – II. The soft-thermal emission

V. Heard[★] and R. S. Warwick

Department of Physics and Astronomy, University of Leicester, University Road, Leicester, LE1 7RH, UK

Accepted 2013 June 15. Received 2013 June 14; in original form 2013 April 25

ABSTRACT

We have extended our earlier study of the X-ray emission emanating from the central 100 pc \times 100 pc region of our Galaxy to an investigation of several features prominent in the soft X-ray (2–4.5 keV) band. We focus on three specific structures: a putative bipolar outflow from the vicinity of Sgr A^{*}; a high surface brightness region located roughly 12 arcmin (25 pc) to the north-east of Sgr A^{*} and a lower surface brightness extended loop feature seen to the south of Sgr A^{*}. We show, unequivocally, that all three structures are thermal in nature and have similar temperatures ($kT \approx 1$ keV). The inferred X-ray luminosities lie in the range $(2\text{--}10) \times 10^{34}$ erg s^{−1}. In the case of the bipolar feature we suggest that the hot plasma is produced by the shock heating of the winds from massive stars within the Central Cluster, possibly collimated by the Circumnuclear Disc. Alternatively the outflow may be driven by outbursts on Sgr A^{*}, which follow tidal disruption events occurring at a rate of roughly one every 4000 yr. The north-east enhancement is centred on a candidate pulsar wind nebula which has a relatively hard non-thermal X-ray spectrum. We suggest that the coincident soft-thermal emission traces the core of a new thermal-composite supernova remnant, designated as SNR G0.13–0.12. There is no clear evidence for an associated radio shell but such a feature may be masked by the bright emission of the nearby Radio Arc and other filamentary structures. SNR G0.13–0.12 is very likely interacting with the nearby molecular cloud, G0.11–0.11, and linked to the *Fermi* source, 2FGL J1746.4–2851c. Finally we explore a previous suggestion that the elliptically shaped X-ray loop to the south of Sgr A^{*}, of maximum extent ~ 45 pc, represents the shell of a superbubble located in the GC region. Although plausible, the interpretation of this feature in terms a coherent physical structure awaits confirmation.

Key words: Galaxy: centre – X-rays: ISM.

1 INTRODUCTION

The central 100-pc of our Galaxy is a fascinating region which abounds with unusual astrophysical features and exotic phenomena. The region is characterized by a high concentration of both stars and interstellar material with the enclosed mass of $\sim 3 \times 10^8 M_{\odot}$ (Launhardt, Zylka & Mezger 2002). The non-stellar component is distributed in dense molecular clouds within a structure known as the Central Molecular Zone (Morris & Serabyn 1996; Molinari et al. 2011). The presence within the region of three of the most massive young star clusters in the Galaxy (Figer, McLean & Morris 1999; Figer et al. 2002; Paumard et al. 2006) is just one of many signatures of recent star formation. An enhanced rate of massive star formation gives rise to supernova (SN) explosions every few

thousand years and hence to a ready supply of heat and accelerated particles (Crocker et al. 2011). These in turn fuel a range of energetic thermal and non-thermal emission processes (e.g. Koyama et al. 1989; Yamauchi et al. 1990; Bélanger et al. 2004; Muno et al. 2004; Crocker et al. 2011; Yusef-Zadeh et al. 2013). A supermassive black hole (SMBH) of mass $(4.5 \pm 0.4) \times 10^6 M_{\odot}$ (Schödel et al. 2002; Ghez et al. 2008; Gillessen et al. 2009) resides at the dynamical centre of the Galaxy; although currently in a quiescent accretion state, the SMBH may, during past outbursts, have further energized the surrounding region (Koyama et al. 1996; Murakami, Koyama & Maeda 2001; Ponti et al. 2010; Nobukawa et al. 2011; Capelli et al. 2012; Gando Ryu et al. 2012). Accretion power also drives the luminous X-ray binaries and transient sources which are very prominent in X-ray and γ -ray observations of the GC (e.g. Sidoli et al. 1999; Muno et al. 2006; Degenaar et al. 2012).

In an earlier paper (Heard & Warwick 2013, hereafter Paper I), we used *XMM–Newton* observations in an investigation of the spatial

[★] E-mail: vh41@le.ac.uk

distribution and spectral characteristics of the extended X-ray emission associated with the central 100-pc region. More specifically, we argued that the very hot thermal emission which is particularly bright in the GC and which can be characterized spectrally as a thermal bremsstrahlung component ($kT \approx 7.5$ keV), plus attendant He-like and H-like iron K-shell lines, is best explained in terms of the integrated emission of unresolved point sources. It seems likely that this population of X-ray sources (with the X-ray luminosity, L_X , of individual sources typically in the range $10^{30} - 10^{33}$ erg s $^{-1}$) is dominated by cataclysmic variables (CVs) (Muno et al. 2006; Revnivtsev et al. 2011; Yuasa, Makishima & Nakazawa 2012). In Paper I we found that a smooth, centrally concentrated spatial model for these unresolved sources accounted for the bulk of the He-like and H-like iron line emission at 6.7 keV and 6.9 keV, respectively, without recourse to a significant contribution from a very hot *truly diffuse* X-ray plasma. The underlying iron fluorescent line emission at 6.4 keV was also broadly accounted for by the unresolved source model, once the bright fluorescing knots associated with specific dense molecular clouds were excluded.

However, this is not the full story since the GC diffuse X-ray emission also exhibits prominent spectral lines due to K-shell transitions in highly stripped ions of elements such as Si, S and Ar, in ratios which can be readily explained in terms of thermal plasma emission at temperatures in the range 0.6–1.5 keV (e.g. Koyama et al. 1989, 1996; Kaneda et al. 1997; Tanaka et al. 2000; Muno et al. 2004; Nobukawa et al. 2010), i.e. a temperature significantly lower than that characterizing the spectrum of the unresolved sources. The spatial distribution of this cooler plasma is far from uniform, consistent with the hypothesis that it is largely generated through the interaction of SN shock fronts with the ambient interstellar matter.

In this paper (Paper II), we extend our study of the X-ray emission emanating from the central 100 pc of the Galaxy to a consideration of several regions which are very bright in the soft X-ray band, as a consequence of their soft-thermal emission. We concentrate on three features: (i) the ‘bipolar’ emission complex which extends 6 arcmin (14 pc) each side of Sgr A* along a perpendicular to the Galactic plane; (ii) the bright emission located between 8 and 15 arcmin (18–35 pc) to the north-east¹ of Sgr A*, centred on the pulsar wind nebula (PWN) G0.13–0.11; and (iii) a putative superbubble of dimension 25×16 arcmin² (45 pc \times 36 pc) located to the south of Sgr A*. In this study we attempt to characterize the properties and spatial distribution of the soft X-ray emitting plasma in these three regions as a step towards charting the activity and processes which have helped shape the extreme GC environment.

In the next section (Section 2) we briefly summarize the *XMM–Newton* observations used in our study and the data reduction techniques we have employed. In Section 3, we present an image of the central 100-pc region in the 2–4.5 keV band and, through the use of latitudinal cuts across images constructed in different wavebands, take an overview of the properties of the soft X-ray emitting plasma present in the region. The next three sections (Sections 4–6) report a more detailed analysis of the three X-ray bright regions identified above. Finally in Section 7 we summarize our results and conclusions. Throughout this work, the distance to the GC is assumed to be 8 kpc (Gillesen et al. 2009).

2 OBSERVATIONS AND DATA REDUCTION

2.1 Image construction and analysis

Full details of the *XMM–Newton* observations used in this analysis and a description of the techniques employed in the reduction of the data from the three EPIC cameras (Strüder et al. 2001; Turner et al. 2001) can be found in Paper I. In brief, a set of 50 pn and 56 MOS-1/MOS-2 observations, giving a total useful exposure of ~ 0.5 Ms and ~ 0.9 Ms, respectively, were used in the construction of a set of mosaicked images centred on (RA, Dec.) = (266:41657, $-29:0787$). The image format comprised 648×648 pixels (4 arcsec pixels), corresponding to a 43.2×43.2 arcmin² field, which at the distance of the GC equates to a projected extent of 100 pc \times 100 pc.

For this work, the mosaicked images were constructed in five ‘broad’ bands covering a nominal total bandpass from 1 to 10 keV (see Table 1). In addition, images were made in a number of ‘narrow’ bands matching prominent spectral lines. Table 1 lists the narrow-band energy ranges used in the present study. These correspond to the K-shell lines of He-like silicon, sulphur and argon, the neutral (or near-neutral) iron fluorescence line at 6.4 keV (Fe I K α), and the K-shell lines at 6.7 keV and 6.9 keV from He-like (Fe xxv K α) and hydrogenic (Fe xxvi Ly α) ions of iron. Narrow-band images sampling a spectral range near to that of each emission line were also produced (see Table 1) and used to subtract the continuum underlying each line (see below).

Paper I describes how we constructed mosaicked images separately for the pn and MOS (MOS 1 + MOS 2) cameras; however,

Table 1. The energy ranges (in keV) of the ‘broad’ bands covering the 1–10 keV bandpass and the ‘narrow’ bands encompassing specific spectral lines.

Broad bands	
Very soft	1.0–2.0
Soft	2.0–4.5†
Hard	4.5–6.0
Iron	6.0–7.2
Very hard	7.2–10.0‡
Narrow bands	
Si xiii K α	1.740–1.920
Cont. Si	1.920–1.965
...	2.070–2.115
S xv K α	2.340–2.550
Cont. S	2.070–2.115
...	2.250–2.310
...	2.700–2.805
Ar xvii K α	3.015–3.225
Cont. Ar	2.910–3.015
...	3.225–3.330
Fe i K α	6.270–6.510
Fe xxv K α	6.525–6.825
Fe xxvi Ly α	6.840–7.110
Cont. Fe low	5.700–6.150
Cont. Fe high	7.200–7.650

† In the equivalent table in Paper I, the 2–4.5 keV bandpass was referred to as the medium (energy) band.

‡ The 7.8–8.3 keV spectral region encompassing the Cu K α instrumental line was excluded in the case of the pn data, whereas for the MOS data the very hard band was truncated at 9.0 keV.

¹ In this paper directions are referenced to the celestial coordinate system unless otherwise specified.

for the image analysis in this paper, all the data have been co-added. The procedure for combining the pn and MOS channels was as follows. First the ratio of the MOS to pn count rate was calculated for each broad-band. This was the field-average value determined from a comparison of the separate pn and MOS images. For each broad-band, the pn, MOS 1 and MOS 2 counts from each observation were co-added into a combined-counts image formatted as described above. Similarly a combined-exposure map was constructed, where both the MOS 1 and MOS 2 contributions were scaled by the (single camera) MOS to pn count rate ratio appropriate to the band. The final flat-fielding step for the broad-bands then involved dividing each combined-counts image by the corresponding combined-exposure map. In the case of the narrow-band image centred on the He-like Si line, we used the 1.0–2.0 keV exposure map in this flat-fielding step. Similarly, for the narrow-band images centred on the He-like S and Ar lines, the 2.0–4.5 keV exposure map was utilized. Finally for the narrow-band images centred on

the three iron lines, we used the 6.0–7.2 keV exposure map. Hereafter we refer to the narrow-band images simply as the Si, S, Ar, Fe64, Fe67 and Fe69 images.

In order to trace the distribution of the line emission, it is necessary to make a correction for the in-band continuum emission underlying the emission lines. For the Si, S and Ar images, a straight subtraction of the appropriate nearby continuum narrow-band image (after applying a suitable scaling for the sampled bandwidth) proved an adequate approximation. See Paper I for a discussion of the continuum-subtraction procedure adopted in the case of the Fe64, Fe67 and Fe69 images and for the approach used to correct for the spillover of each iron line into the adjacent narrow bands.

By way of illustration, Fig. 1 shows the combined pn/MOS mosaicked image for the soft X-ray (2.0–4.5 keV) band after applying both a source mask and light spatial smoothing. The source mask was designed to exclude a significant fraction (>80 per cent) of the signal from discrete sources with X-ray luminosity $>10^{33}$ erg s $^{-1}$

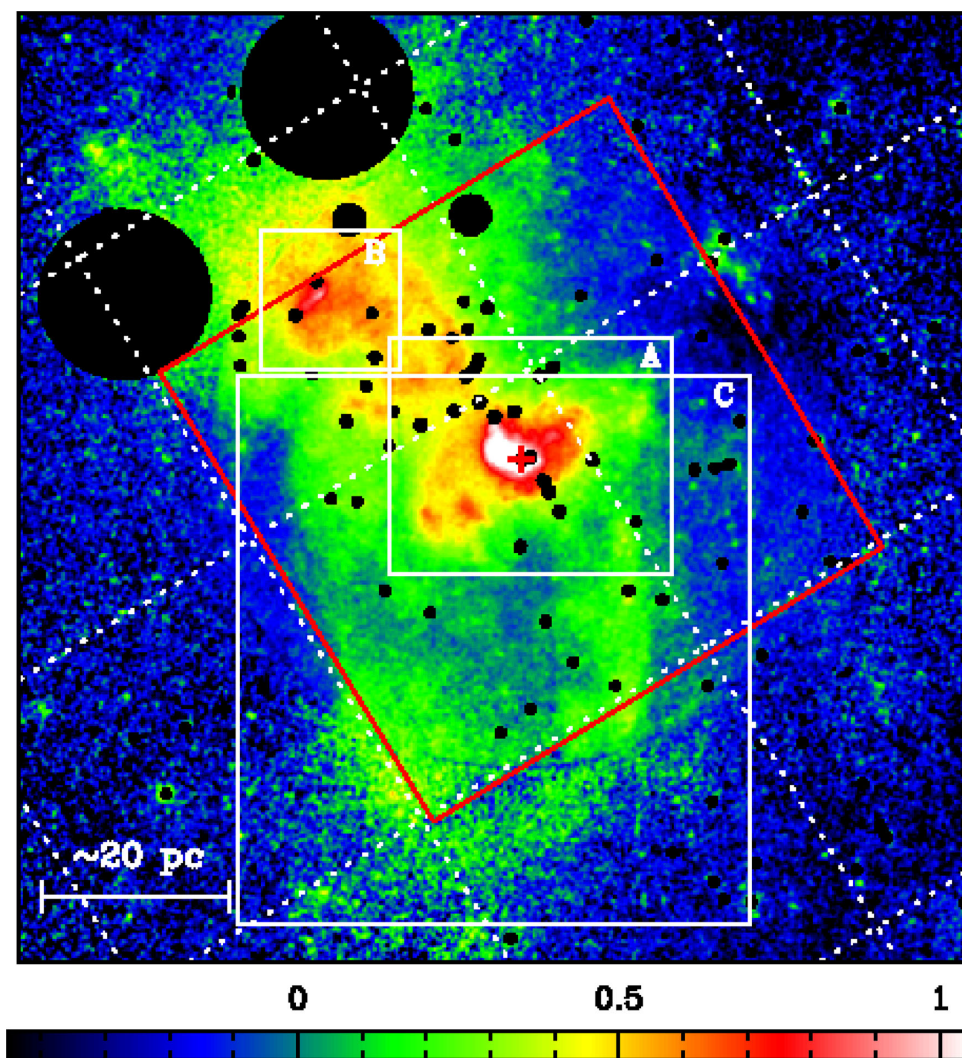


Figure 1. Combined pn/MOS mosaicked image in the 2.0–4.5 keV band covering the central 43.2×43.2 arcmin 2 field of the GC (100 pc \times 100 pc at the GC distance). The mosaic is constructed on a celestial coordinate grid with east to the left. The intensity scaling is logarithmic; the colour bar shown at the bottom of the figure is calibrated in units of $\log_{10}(\text{count}/20 \text{ ks}/\text{pixel})$. The image has been spatially smoothed using a circular Gaussian function of width $\sigma = 1$ pixel (1 pixel = 4 arcsec). A source mask has been applied so as to exclude the bulk of the signal from luminous discrete sources (see text). The white dotted lines represent a Galactic coordinate grid with a 15 arcmin spacing. The red box centred on Sgr A* (the position of which is marked by the red cross) indicates the region over which the latitudinal cuts were calculated (see Section 3.2). The white boxes indicate the regions within which individual soft-thermal features are contained (see Sections 4–6).

(2–10 keV). A few modifications were made to the mask employed in Paper I, namely: (i) the current mask excludes the peak emission of the central star cluster, which has Sgr A* at its core; however it does not remove the extended emission associated with the Sgr A East supernova remnant (SNR); (ii) extended continuum emission directly associated with the PWN G0.13–0.11 is not excised; (iii) faint emission associated with the Quintuplet cluster is now masked out. The impact of the masking is most evident in the north-east corner of the image, where large excision circles mark the locations of two very luminous sources, the X-ray transient SAX J1747.0–2853 (Wijnands, Miller & Wang 2002; Degenaar et al. 2012) and the persistent source 1E 1743.1–2843 (Porquet et al. 2003; Del Santo et al. 2006). In this same region the two mid-sized excision circles correspond to the Quintuplet and Arches star clusters (Yusef-Zadeh et al. 2002b; Law & Yusef-Zadeh 2004).

2.2 Spectral extraction and modelling

For the current work, the X-ray spectral analysis was largely based on a single pn observation (0202670801) for which the exposure time after filtering was ~ 62 ks. The one exception to this was the investigation of G359.79–0.26 (see Section 6), which was outside of the field of view. In this case, we used an alternative observation (0112971001) for which the exposure time after filtering was ~ 7 ks. The *XMM-Newton* SAS v11.0 (hereafter SAS) was used to extract the data and generate all the instrument response files required for the spectral analysis.

The wide extent and complex morphology of the diffuse soft X-ray emission in the GC field make the selection of a suitable background region for use in spectral analysis extremely problematic. We have therefore followed the same approach to background subtraction as described in Paper I, and made use of EPIC filter wheel closed (FWC) data. FWC spectra were extracted from geometrical areas on the pn detector matching those utilized in the actual observations and then scaled by the ratio of the exposure times of the observation and FWC data sets. The use of these FWC spectra as background data sets proved fully satisfactory for our application, namely the study of GC regions of relatively high, soft X-ray surface brightness. One consequence of using FWC data as the background estimator is that the applied spectral model should, in principle, include emission associated with both the Galactic foreground and the cosmic X-ray background, as well as with the GC. However, in practice, the contribution of the cosmic X-ray background was negligible, whereas constraints of any foreground contribution were provided by the measurements of the net line-of-sight column density, N_{H} .

In Paper I, we discussed how the GC X-ray spectra could be modelled in terms of just three major emission components. The first is the emission associated with the unresolved hard X-ray emitting point sources (with $L_{\text{X}} < 10^{33}$ erg s $^{-1}$, 2–10 keV). Here we follow the same approach as in Paper I and represent this component as a bremsstrahlung continuum plus four Gaussian lines representing the iron fluorescence components, Fe I $K\alpha$ and $K\beta$, and the K-shell lines of Fe xxv and Fe xxvi. The temperature of the bremsstrahlung was fixed at 7.5 keV and the absorbing column density set at $N_{\text{H}} = 12 \times 10^{22}$ cm $^{-2}$. The line equivalent widths were set to 235, 735 and 290 eV for the neutral Fe $K\alpha$ and the He-like and H-like Fe lines, respectively (these are the average values for the Lat +ve and Long –ve region in Paper I, table 5). The normalization of the neutral Fe $K\beta$ line was fixed at 11 per cent of that of the $K\alpha$ line (Koyama et al. 2009). The line energies and intrinsic widths were fixed at the values employed in Paper I. In the spectral fitting, the

only free parameter was the normalization of the bremsstrahlung continuum.

The second emission component relates to the reprocessing of incident X-ray photons in dense molecular clouds in the GC. The most obvious signature is the Fe $K\alpha$ fluorescence line at 6.4 keV (Koyama et al. 2007a, 2009; Yusef-Zadeh et al. 2007; Ponti et al. 2010; Capelli et al. 2012), with the Thomson scattering of the incident X-ray flux giving rise to an associated hard continuum. Here we model the latter as a power-law continuum with a photon index fixed at a value of 1.8. The iron fluorescence was represented as a combination of Fe $K\alpha$ and $K\beta$ emission (from neutral or near-neutral matter). For this component, the equivalent width of the 6.4 keV line was fixed at 1600 eV (an average value for the Long +ve region studied in Paper I). As before, the normalization of the $K\beta$ line was set equal to 11 per cent of that of the $K\alpha$ value. The absorbing column applied to the power-law continuum was fixed at 12×10^{22} cm $^{-2}$. Again, the only free parameter in the spectral fitting was the normalization of the continuum.

The third component represents the soft X-ray emission emanating from the diffuse thermal plasma which pervades the GC region. In the present work, the starting point for the spectral analysis was to assume conditions of thermal and ionization equilibrium and that the soft-thermal emission could be adequately represented by a single-temperature *VAPEC* component in *XSPEC* (Arnaud 1996). In the spectral fitting the plasma temperature, kT , and normalization remained free parameters as did the absorbing column density, N_{H} . The relative abundances of Si, S and Ar were also allowed to vary.²

In the spectral analysis, raw spectral channels were grouped so as to give a minimum of 20 counts per bin. Uncertainties on the derived spectral parameters are quoted at the 90 per cent confidence range unless otherwise stated. All spectral modelling was carried out utilizing the X-ray spectral-fitting package (*XSPEC* v12.7.0, Arnaud 1996). Throughout this paper we assume the solar abundance values of Anders & Grevesse (1989). Further details of the fitting of the spectra extracted from specific regions are given in later sections.

3 SOFT-THERMAL EMISSION IN THE GC

3.1 Overview

A number of distinct spatially extended structures are apparent in Fig. 1, on scales ranging from sub-parsec up to tens of parsec (e.g. Baganoff et al. 2003; Morris et al. 2003; Munro et al. 2003, 2004; Park et al. 2004). The brightest feature near the centre of the image is the Sgr A East SNR (Maeda et al. 2002; Sakano et al. 2004; Koyama et al. 2007b). Beyond this, the soft X-ray emission within a radius of about 6 arcmin of Sgr A* appears to have a clumpy ‘bipolar’ morphology with a long axis orientated roughly perpendicular to the Galactic plane (Fig. 1, region A) – see Section 4. The soft X-ray emission is also significantly enhanced to the NE of Sgr A* (Fig. 1, region B). Here, the spatial morphology is rather complex with evidence for several narrow filamentary features. The surface brightness peaks at the location of a discrete source (G0.13–0.11) previously described as a potential PWN (Wang, Lu & Lang 2002). We will discuss the nature of the emission in this region in Section 5. The final distinct large-scale structure evident in Fig. 1 lies to the south of Sgr A*, in the form of an elongated loop feature which

²The abundances of all the other metals were fixed at the solar value, since useful constraints on these parameters could not be derived from the available data.

is apparent in the lower surface brightness emission (Fig. 1, region C). Mori et al. (2009) have interpreted this feature as a superbubble – we will consider this possibility in Section 6.

3.2 Latitudinal cuts

We have explored the general properties of the GC soft X-ray emission by taking cuts in Galactic latitude through several of the broad-band images and also through a number of the narrow-band spectral-line images. The region considered is that shown in Fig. 1 (as the red box) which is centred on Sgr A* and has an extent of ± 12 arcmin in both the Galactic latitude and longitude directions. The resulting cuts represent count rate averages over longitude, sampled at a 30 arcsec spacing in latitude. Throughout this section we reference the latitude offset to the plane that passes through Sgr A*.

The cuts through the 2–4.5 and 4.5–6 keV images peak at the position of Sgr A East SNR (Fig. 2a). The surface brightness in these bands falls off sharply with the latitude offset, albeit with a distinct ‘pedestal’ of emission at offset angles between -1 and -6 arcmin. In the 1–2 keV band, Sgr A East is much less prominent and the

emission distribution is somewhat flatter than that seen at higher energies. This suggests that the contribution from a region (or regions) located in front of the GC (where N_H is somewhat reduced) may be significant, particularly outside of the central ~ 5 arcmin radius zone.

Similar patterns can be traced in the cuts deriving from the Si, S and Fe67 images (Fig. 2b). The Sgr A East SNR is a very bright source in the Fe67 image but makes little contribution in the lower energy lines (Maeda et al. 2002; Sakano et al. 2004; Koyama et al. 2007b). The distribution of the S-line emission falls off steeply towards +ve offset, but less so towards –ve offset. In contrast, the Si-line emission generally has a flatter distribution, particularly at –ve offset. The fact that both emission lines are bright across the full field confirms that soft-thermal emission pervades the region. Of the three lines, the Fe67 distribution is most symmetric with respect to the latitudinal offset from Sgr A*. As noted in Paper I, much of this Fe-line flux can be accounted for in terms of the integrated emission of unresolved low-luminosity sources. In the figure we show the estimated contribution to the Fe67 emission of the unresolved sources, as determined by the source model reported

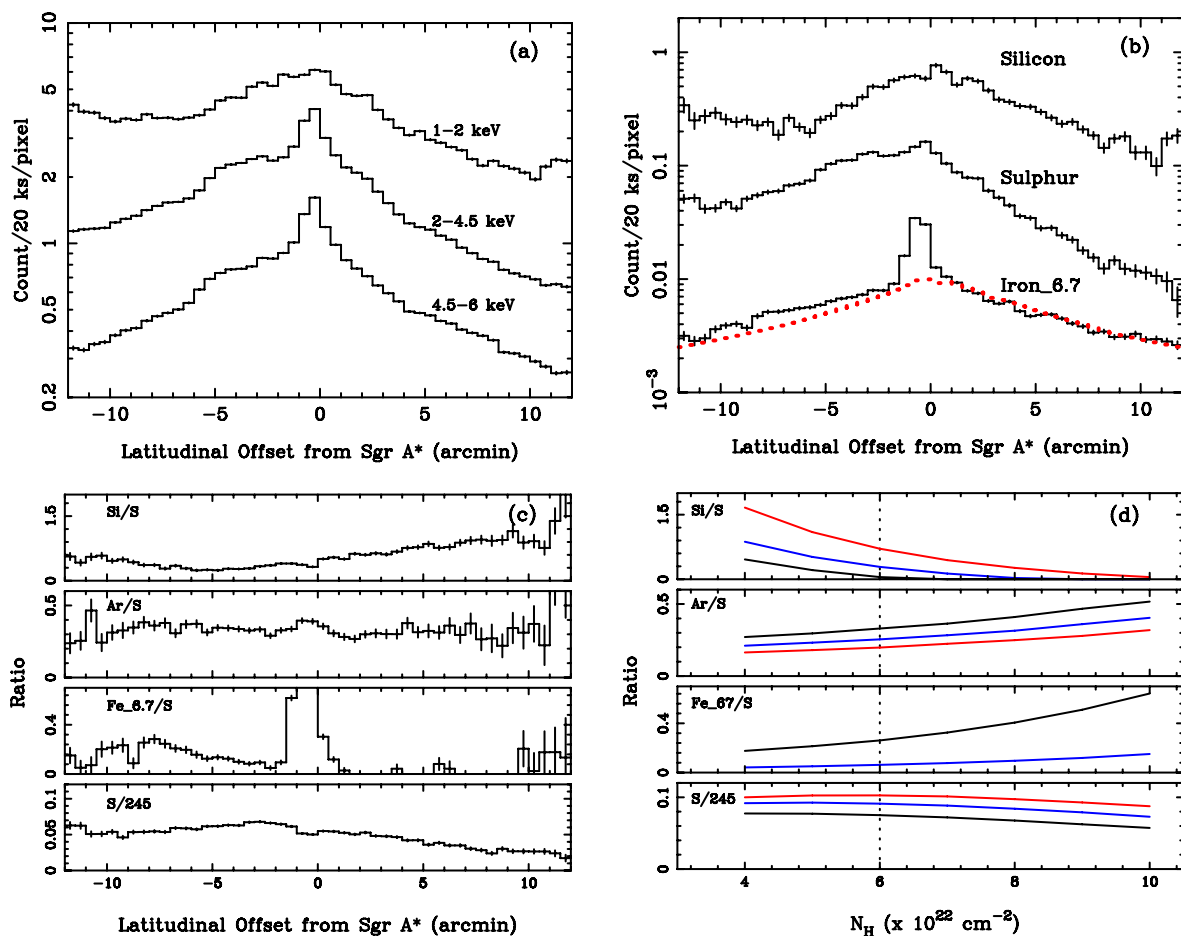


Figure 2. Spatial cuts along the direction of Galactic latitude for a 12×12 arcmin² region centred on Sgr A*. Upper-left (a): the distribution of soft continuum emission in the three ‘broad’ bands encompassing the 1–6 keV energy range. For clarity, the 1–2 keV distribution has been shifted upwards by a factor of 10. Upper-right (b): the distribution of the emission in three narrow bands corresponding to the He-like Si, He-like S and He-like Fe K-shell lines. Again for clarity, the Si-line (Fe-line) distribution has been shifted upwards (downwards) by a factor of 10. The dotted red line indicates the unresolved-source contribution to the He-like Fe line (see text). Lower-left (c): various count rate ratios as follows: Si/S; Ar/S, (He-like) Fe/S (with the unresolved source contribution to the iron emission subtracted). Also shown is the fractional contribution of the S line to the 2–4.5 broad-band emission. Lower-right (d): the predicted ratios as a function of the assumed line of sight N_H for thermal plasmas at temperatures, kT , of 0.8 keV (red line), 1.0 keV (blue line) and 1.2 keV (black line). The vertical dashed line is drawn at $N_H = 6 \times 10^{22} \text{ cm}^{-2}$, the nominal line-of-sight column density to the GC.

in Paper I. Clearly, this model accounts for virtually all of the observed emission at +ve offset, although a modest excess is evident at -ve offset (-2 to -10 arcmin). In Paper I we interpreted this excess He-like iron emission as arising from thermal plasma with a temperature extending up to 1.5 keV, i.e. a somewhat hotter temperature component than is the norm for the GC region. We will return to this point shortly.

Fig. 2(c) compares the signal recorded in several bands to that observed in the case of the S line, with Fig. 2(d) providing a calibration of the measured ratios in terms of various *VAPEC* thermal models. In this latter plot, the x -axis has N_H ranging from $(4-10) \times 10^{22} \text{ cm}^{-2}$ and the three curves corresponding to plasma temperatures, kT , of 0.8, 1.0 and 1.2 keV. All the models assume solar abundances.

The Si/S ratio reaches a minimum value of 0.24 at -ve offset, consistent with a 1-keV thermal component absorbed by $N_H = 6 \times 10^{22} \text{ cm}^{-2}$ (the nominal GC column density assumed by Muno et al. 2004). The rise in the Si/S ratio towards +ve offset can be matched by a reduction in the net line-of-sight column to $N_H \sim 4 \times 10^{22} \text{ cm}^{-2}$. This might be explained either in terms of a reduction in the column density affecting the bulk of GC plasma or due to an increasing contribution from the foreground emission as the GC component falls off with latitude. The Ar/S ratio remains reasonably constant across the whole field at a value of ~ 0.3 ; this again matches a thermal component with a temperature of roughly 1 keV with the nominal GC N_H . The Fe67 excess peaks around -8 arcmin, with a Fe67/S ratio commensurate with a (somewhat enhanced) plasma temperature of about 1.2 keV. Alternatively a blend of temperatures from, say, 1 to 1.5 keV could also explain the observed He-like iron excess.³

Figs 2(c) and (d) also show the S/245 ratio, that is the contribution of the S line to the 2–4.5 keV broad-band signal. The measured ratio peaks at a value of ~ 0.07 at -ve offset and then declines at +ve offsets to a value of ~ 0.03 . In contrast, the predicted fraction for our fiducial thermal model ($kT = 1 \text{ keV}$, $N_H = 6 \times 10^{22} \text{ cm}^{-2}$) is 0.095. This discrepancy is readily explained if the contribution of unresolved sources to the measured 2–4.5 keV broad-band signal is roughly 30 per cent in the region where the S/245 ratio is at its peak value, ranging up to a 70 per cent contribution at the northern boundary of the region studied.

4 A BIPOLAR OUTFLOW FROM SGR A*?

4.1 Images of the central region

Fig. 3(a) shows a zoomed-in version of the 2–4.5 keV image covering a central $12.9 \times 10.7 \text{ arcmin}^2$ ($30 \text{ pc} \times 25 \text{ pc}$) region. As noted previously the brightest extended object in the field is the Sgr A East SNR. On a somewhat larger scale, the emission distribution appears to be elongated along an axis perpendicular to the Galactic plane. The twin conical regions defined by the diagonal lines in the figure (with an apex at the location of Sgr A* and an opening half-angle of 20°) encompass several of the bright features which, in effect, delineate this elongated structure. This includes a ‘ridge’ of high surface brightness extending approximately 2 arcmin (4.6 pc) to the north-

west and two obvious bright clumps located between 3 and 6 arcmin (7–14 pc) to the south-east. A further isolated lower-surface brightness ‘cloud’ is also present in the north-west sector. These features are also evident in the radial profile of the emission shown in Fig. 4. This figure highlights the presence of an asymmetry in the emission distribution, namely that the radial profile to the north-west is markedly steeper than that to the south-east. As previously reported by Sidoli & Mereghetti (1999), an elongated structure similar to that seen in X-rays is also apparent in the synchrotron halo of Sgr A, as revealed in 90 cm radio observations (LaRosa et al. 2000; Nord et al. 2004). Finally we note that a further arc-like feature is evident in the *XMM-Newton* images. This structure extends to the south-east, from its starting point at the eastern boundary of the Sgr A East SNR, over a length scale of at least 2.5 arcmin (6 pc).

Fig. 3(b) shows for comparison the S+Ar line image obtained by co-adding the individual S and Ar images of this central region. The same features, as noted above, are bright in this line image, demonstrating their soft-thermal nature. We have investigated the spectra of the three regions defined by black rectangles in the line image, labelled as the NW, SE and E regions; these encompass, respectively, the north-west ridge, the two south-east clumps and the arc-like feature.

4.2 Spectral constraints

The spectra extracted from the three regions identified above can be modelled assuming just two emission components, namely the emission from unresolved sources and soft-thermal emission (see Section 2.2). The resulting best-fitting parameters pertaining to the thermal plasma emission are reported in the first three columns of Table 2. Fig. 5 shows the corresponding best-fitting spectra and residuals. The two-component model provides a reasonable fit to the data in all three regions, although systematic trends in the residuals, particularly below 2 keV, emphasize the approximate nature of our single-column, single-temperature, thermal model. The plasma temperature characterizing the three regions is not too far from the 1-keV fiducial discussed in Section 3.2, although the temperature measured in the SE region is marginally hotter than that in the other two regions (by $\sim 0.2 \text{ keV}$). In Fig. 5, this higher temperature is most evident in terms of the enhanced line emission near 6.7 keV (comparing the modelled spectrum of the SE region with that of the NW and E regions) due to the Fe-K emission of highly stripped iron ions up to helium-like states. The absorption column density measured for the NW region is somewhat higher than that determined for the SE and E regions and also higher than the nominal column density of $6 \times 10^{22} \text{ cm}^{-2}$ reported for the GC. One interpretation of this additional absorption might be that the north-east ridge lies behind the plane of Sgr A*. If this were the case then it would imply that the northern component of the elongated structure is tipped both away from us and away from the normal to the Galactic plane (see below). Of course, the additional absorption may simply be a manifestation of the complex distribution of molecular gas in the immediate foreground of the Sgr A region. A further result from the spectral fitting is that the relative abundances determined for Si, S and Ar are near to solar values for all three regions.

Using the results from Table 2, we have calculated the physical parameters of the X-ray emitting plasma contained within the NW, SE and E regions (see Table 3). In each case we assumed that the dimension of the emitting region in the direction along the line of sight was equal to that of the smaller dimension of the defining rectangle (see Table 2). The X-ray luminosities are determined from

³ The centroid of the iron-line complex pertaining to a plasma with a temperature in the range 1–1.5 keV peaks below 6.7 keV, indicative of a range of ionization states below that of He-like iron. Nevertheless, a significant signal will still be recorded in our narrow-band He-like Fe channel. There will also be some spillover into the 6.4 keV narrow band, which may explain the modest 6.4-keV excess at -ve offset evident in fig. 4 of Paper I.

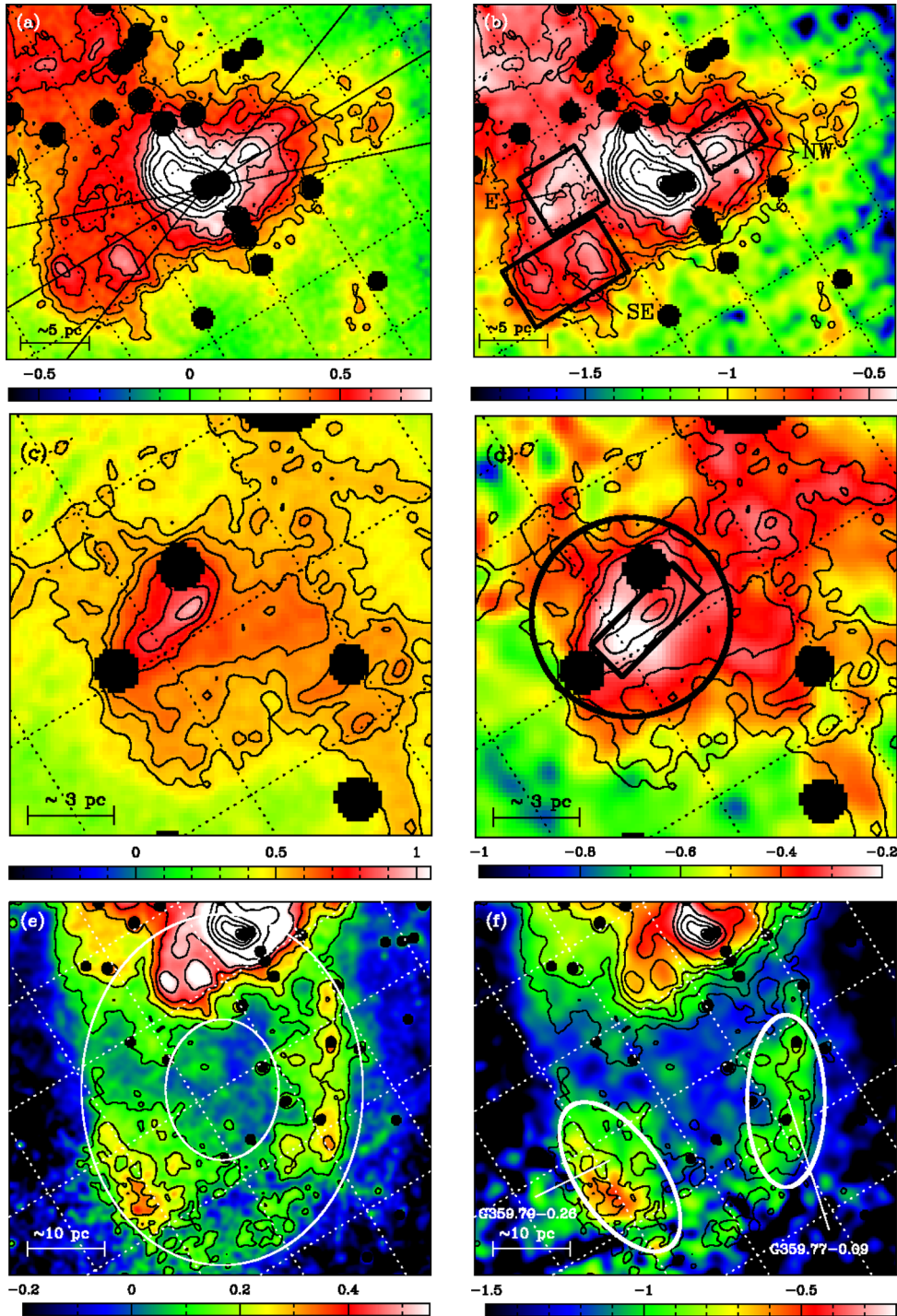


Figure 3. (a) 2–4.5 keV image of the central 12.9×10.7 arcmin² region. The solid diagonal lines are orientated at -20° , 0° and $+20^\circ$ relative to a line of constant longitude passing through Sgr A*. (b) Combined S and Ar (S+Ar) image of the same region as in (a), with contours derived from the 2–4.5 keV image. The rectangles labelled NW, SE and E indicate the regions from which spectra were extracted. (c) 2–4.5 keV image of the north-east enhancement region covering a 6.3×6.3 arcmin² field. (d) The S+Ar image of the same region as in (c), with contours derived from the 2–4.5 keV image. The rectangle represents the spectral extraction region for the PWN G0.13–0.11, whereas the circle defines the spectral extraction extent for the surrounding nebulosity. (e) 2–4.5 keV image of the superbubble region covering a 23×21 arcmin² field. The two ellipses define the possible extent of the superbubble structure (see text). (f) The S+Ar image of the same region as in (e), with contours derived from the 2–4.5 keV image. The two small ellipses encompass the features designated as G359.77–0.09 and G359.79–0.26 for which spectra were extracted. In all the images the intensity scaling is logarithmic, with the colour bar shown at the bottom of each panel having units of \log_{10} (count/20 ks/pixel). The diagonal dotted lines represent a Galactic coordinate grid with 2.4 arcmin spacing in (a)–(d) and 4.8 arcmin spacing in (e)–(f). The continuum images have been spatially smoothed using a Gaussian function of width $\sigma = 4$ arcsec, whereas for the S+Ar images $\sigma = 10$ arcsec (except for the superbubble region where the image smoothing parameters were $\sigma = 10$ arcsec and $\sigma = 20$ arcsec, respectively). The filled black circles correspond to sources excised by the spatial mask.

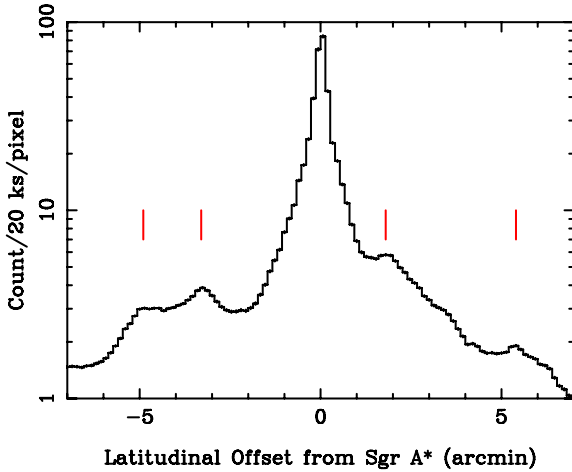


Figure 4. The radial distribution of the 2–4.5 keV emission within the bounds of the conical regions shown in Fig. 3(a). The vertical lines drawn at offset angles of -4.9 , -3.3 , $+1.8$ and $+5.4$ arcmin mark the positions of the two SE clumps, the NW ridge and the isolated NW cloud, respectively.

the unabsorbed fluxes quoted in Table 2. A number of the physical parameters depend on the volume filling factor of the emitting plasma (f) as indicated. The cooling time ($t_{\text{cool}} = E_{\text{th}}/L_{\text{bol}}$) was determined assuming an L_{bol}/L_X ratio of 20, which has an associated uncertainty of about 50 per cent (Muno et al. 2004).

The parameter values pertaining to the hot plasmas in the three regions are fairly similar. The inferred electron densities are in the range $4\text{--}10\text{ cm}^{-3}$ (assuming f is of the order of unity), which is higher than is typical of the GC in general (e.g. Muno et al. 2004; Koyama et al. 1996). The total mass of hot plasma contained within each region is roughly $1\text{--}2 M_{\odot}$. Similarly the radiative cooling time-scales are all in the range $(5\text{--}10) \times 10^5$ yr.

4.3 Origin of the bipolar morphology

An early glimpse of the distribution of the diffuse soft X-ray emission present in the Sgr A region was provided by *BeppoSAX* observations (Sidoli & Mereghetti 1999). More recently, *Chandra* has resolved this emission into a variety of sub-components, including a number of features which form an apparent elongated structure centred on Sgr A* aligned perpendicular to the Galactic plane (Baganoff

et al. 2003). These authors have suggested that the features may, collectively, be evidence of a hot and clumpy ‘bipolar’ outflow from Sgr A* – see also Morris et al. (2003) and Markoff (2010). Our present *XMM-Newton* observations further delineate the morphology of this structure and also demonstrate, unequivocally, the thermal nature of the X-ray emission.

In the bipolar outflow scenario, hot plasma produced within the central few parsec is simultaneously driven outwards and collimated into a channelled flow. One possibility is that the X-ray emitting plasma is produced by shock heating when the high-velocity winds of the many massive Wolf–Rayet and supergiant OB stars within the Central Cluster (Genzel et al. 2003; Paumard et al. 2006; Martins et al. 2007) collide with each other and with the surrounding interstellar medium (ISM). Rockefeller et al. (2004) have shown that such a wind can fully account for the diffuse X-ray luminosity observed within the inner 10 arcsec (0.4 pc) of the Galaxy and furthermore predicted a plasma temperature of $kT \approx 1.3$ keV. As suggested by Markoff (2010), the resulting outflow might then be concentrated into twin ‘lobes’ by the 2-pc radius ring of dense molecular gas which defines the inner extent of the Circumnuclear Disc (CND; Christopher et al. 2005; Oka et al. 2011). Interestingly, the orbital plane of this dense molecular ring (position angle with respect to the Galactic plane $p \sim 0^\circ$ and inclination to our line of sight $i = 50^\circ\text{--}75^\circ$) is well matched to the alignment of the bipolar X-ray structure. One issue with this hypothesis is the question of how the sub-structure within the bipolar flow might have formed if the wind from the Central Cluster has been quasi-continuous over the cluster lifetime of 6 ± 2 Myr (Paumard et al. 2006).

Since the X-ray emitting plasma which forms the wind is likely to be over-pressured with respect to its surroundings, adiabatic losses may dominate over radiation cooling. A plasma temperature of approximately 1 keV gives a sound speed $v_s = (kT_e\gamma/\mu m_H)^{1/2} \approx 500\text{ km s}^{-1}$ (assuming energy equipartition between the electrons and ions, $\gamma = 5/3$ and $\mu = 0.6$). On the basis of a 20° half-opening angle for the bipolar structure, we can estimate the transport velocity within the outflow to be $\sim 500 \times \text{cosec}(20^\circ)\text{ km s}^{-1}$, i.e. $\sim 1500\text{ km s}^{-1}$. However, this estimate will be an upper limit if the outflow is at least partly confined by the dense clouds located along the track of the outflow outside of the CND region. By way of comparison, the terminal winds for the most massive stars in the Central Cluster range from 500 to 2500 km s^{-1} , with the average being $\sim 1000\text{ km s}^{-1}$ (Martins et al. 2007).

Table 2. The best-fitting spectral parameters for the thermal emission seen in the NW, SE, E, G0.13–0.12, G359.77–0.09 and G359.79–0.26 regions.

	Bipolar outflow			SNR	Superbubble	
	NW	SE	E	G0.13–0.12	G359.77–0.09	G359.79–0.26
Area (arcmin ²)	1×0.7	1.7×1	1×1	$\pi 1.5^2$	4.8×2.2	4.8×2.4
N_H ($\times 10^{22}\text{ cm}^{-2}$)	$8.0^{+0.6}_{-0.5}$	$6.3^{+0.3}_{-0.3}$	$6.3^{+0.4}_{-0.4}$	$5.6^{+0.4}_{-0.4}$	$5.9^{+0.3}_{-0.2}$	$4.4^{+0.5}_{-0.4}$
kT (keV)	$0.91^{+0.06}_{-0.05}$	$1.14^{+0.06}_{-0.05}$	$0.96^{+0.07}_{-0.06}$	$1.1^{+0.1}_{-0.1}$	$0.73^{+0.04}_{-0.04}$	$1.02^{+0.15}_{-0.08}$
Z_{Si} (Z_{\odot})	$1.0^{+0.4}_{-0.3}$	$0.6^{+0.2}_{-0.2}$	$0.7^{+0.3}_{-0.2}$	$1.4^{+0.5}_{-0.3}$	$0.6^{+0.1}_{-0.1}$	$1.1^{+0.4}_{-0.3}$
Z_{S} (Z_{\odot})	$0.7^{+0.1}_{-0.1}$	$0.7^{+0.1}_{-0.1}$	$1.2^{+0.2}_{-0.2}$	$2.0^{+0.8}_{-0.5}$	$0.7^{+0.1}_{-0.1}$	$1.3^{+0.3}_{-0.3}$
Z_{Ar} (Z_{\odot})	$0.6^{+0.3}_{-0.3}$	$0.9^{+0.3}_{-0.3}$	$1.5^{+0.5}_{-0.5}$	$3.4^{+1.7}_{-1.0}$	$1.0^{+0.4}_{-0.3}$	$2.3^{+1.0}_{-0.9}$
Norm. ($\times 10^{-2}$)	$2.1^{+0.4}_{-0.4}$	$1.6^{+0.2}_{-0.2}$	$1.2^{+0.2}_{-0.3}$	$1.0^{+0.7}_{-0.9}$	$4.9^{+1.1}_{-1.0}$	$2.8^{+1.0}_{-0.9}$
F_{2-10} ($10^{-12}\text{ erg s}^{-1}\text{ cm}^{-2}$) ^a	$0.7^{+0.1}_{-0.1}$	$1.1^{+0.1}_{-0.1}$	$0.6^{+0.1}_{-0.1}$	$1.1^{+0.3}_{-0.3}$	$1.2^{+0.3}_{-0.2}$	$2.6^{+0.7}_{-0.8}$
F_{2-10} ($10^{-12}\text{ erg s}^{-1}\text{ cm}^{-2}$) ^b	$3.2^{+0.6}_{-0.6}$	$3.7^{+0.5}_{-0.5}$	$2.1^{+0.4}_{-0.6}$	$3.1^{+0.9}_{-0.9}$	$4.4^{+1.0}_{-0.9}$	$6.5^{+1.9}_{-2.1}$
χ^2/ν	533/511	862/724	547/479	543/558	804/824	208/191

^aThe absorbed flux in the 2–10 keV band.

^bThe unabsorbed flux in the 2–10 keV band.

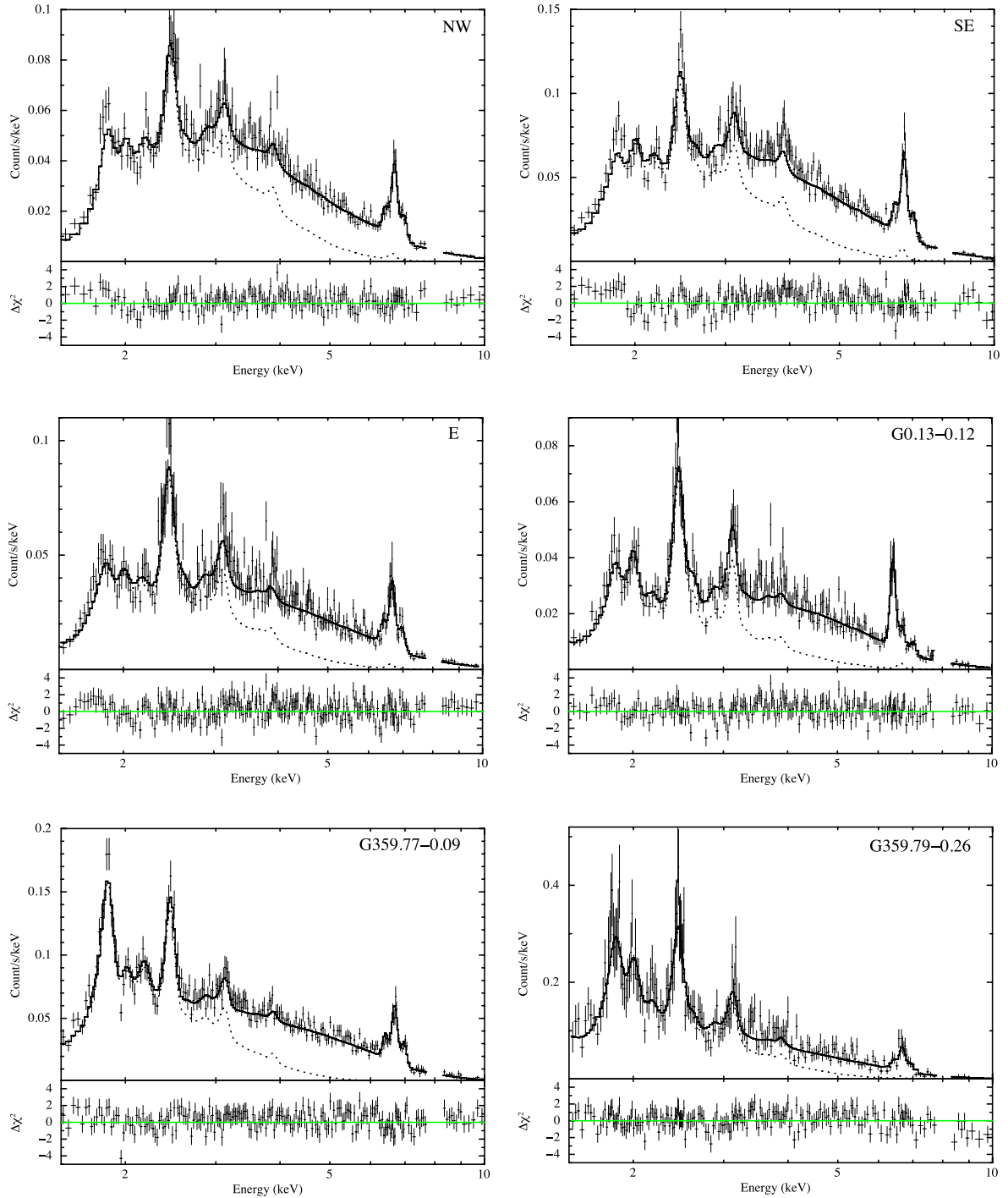


Figure 5. Best-fitting pn spectra of the six regions. In each case the spectral data and best-fitting composite model (solid black line) are shown together with the contribution of the soft-thermal emission to the fit (dotted line). The residuals to the best-fitting model are also shown. From left to right, top to bottom the panels show the results for the NW, SE, E, G0.13–0.12, G359.77–0.09 and G359.79–0.26 regions.

Assuming the transport velocity is 1000 km s^{-1} , the time-scale for plasma to reach the 6 arcmin (14 pc) outer extent of its flow is $\sim 13\,000 \text{ yr}$, which is over an order of magnitude shorter than the inferred radiative cooling time-scale of the plasma clumps (Table 3). This is consistent with the assumption that the adiabatic losses eventually caused the X-ray emitting plasma to dissipate. The kinetic energy contained within the winds of the Central Cluster stars is at least $8 \times 10^{38} \text{ erg s}^{-1}$ (summing over the 18 stars listed in table 2 of Martins et al. 2007). Furthermore, the modelling

of Rockefeller et al. (2004) shows that as much as 26 per cent of the total wind energy within the central parsec can be converted to the internal energy of the plasma via multiple shocks. For comparison, the combined X-ray luminosity of the NW ridge and SE clumps is $\sim 5 \times 10^{34} \text{ erg s}^{-1}$, whereas for the whole bipolar structure the value will be perhaps a factor of 2 higher (excluding the central few parsec where the Sgr A East SNR dominates). The observed X-ray emission thus represents only a tiny fraction ($\sim 10^{-4}$) of the available wind energy. However, the thermal energy stored within

Table 3. Physical parameters of the soft-thermal emission associated with the various regions.

	Bipolar outflow			SNR G0.13–0.12	Superbubble	
	NW	SE	E		G359.77–0.09	G359.79–0.26
Volume, V (cm ³)	1.6×10^{56}	5.5×10^{56}	3.3×10^{56}	4.8×10^{57}	3.2×10^{58}	3.7×10^{58}
Temperature, T (K)	1.1×10^7	1.3×10^7	1.1×10^7	1.3×10^7	8.5×10^6	1.2×10^7
Emission integral, EI (cm ^{−3})	1.5×10^{58}	1.2×10^{58}	8.7×10^{57}	7.2×10^{57}	3.6×10^{58}	2.0×10^{58}
2–10 keV luminosity, L_X (erg s ^{−1})	2.3×10^{34}	2.7×10^{34}	1.5×10^{34}	2.2×10^{34}	3.2×10^{34}	4.7×10^{34}
Electron density, n_e (f ^{−1/2} cm ^{−3})	9.9	4.6	5.2	1.2	1.1	0.7
Thermal energy, E_{th} (f ^{1/2} erg)	6.7×10^{48}	1.4×10^{49}	7.8×10^{48}	3.1×10^{49}	1.2×10^{50}	1.3×10^{50}
Mass, M (f ^{1/2} M _⊙)	1.3	2.1	1.4	5.0	28	23
Pressure, P (f ^{−1/2} dyn cm ^{−2})	2.9×10^{-8}	1.7×10^{-8}	1.6×10^{-8}	4.3×10^{-9}	2.5×10^{-9}	2.3×10^{-9}
Cooling time-scale, t_{cool} (f ^{1/2} yr)	4.6×10^5	8.2×10^5	8.1×10^5	2.2×10^6	5.9×10^6	4.5×10^6

the NW ridge and SE clumps amounts to $\sim 2 \times 10^{49}$ erg (assuming $f \approx 1$), which is roughly half of their bulk kinetic energy if the outflow velocity is ~ 1000 km s^{−1}. For comparison the wind from the Central Cluster releases a total energy of $\sim 3 \times 10^{50}$ erg over a time-scale of 13000 yr. The implication is that the putative outflow stores a substantial fraction of the energy deposited by the central wind into its surroundings.

An alternative explanation for the origin of the outflow is that it is driven by intermittent outbursts on Sgr A* (Markoff 2010). In this scenario, Sgr A* remains in a quiescent state, apart from, on a rare occasions, when a star or cloud passes close enough to the SMBH to give rise to a tidal disruption event. The energy released as matter is accreted on to the SMBH might then drive a wind along the axis of a putative accretion disc, although whether this would result in a bipolar configuration aligned roughly perpendicular to the Galactic plane remains an open question. Alternatively the CND might again provide the requisite collimation. To zeroth order, the X-ray emitting clumps are spaced at radial intervals of ~ 1.7 arcmin (4 pc; see Fig. 4). If we again assume an outflow velocity of 1000 km s^{−1} then the implied time interval between successive tidal disruption events is ~ 4000 yr. This compares with theoretical estimates of the tidal disruption rate of $\sim 10^{-4}$ yr^{−1} (Alexander 2005).

Previous X-ray studies of this region have not specifically identified the arc-like feature which can be traced from the eastern boundary of the Sgr A East SNR towards the south-east. The total extent of this arc is at least 2.5 arcmin (6 pc). The morphology and orientation of the arc suggests a possible connection with the outer SE clump. Spectral analysis (of region E) further confirms that the X-ray emission is thermal in nature with similar properties to the SE clumps. Unfortunately the origin of this arc remains unclear.

5 A NEW SNR CANDIDATE IN THE GC?

5.1 Images of the north-east enhancement

Fig. 3(c) shows the 2–4.5 keV image of the 6.3×6.3 arcmin² (14.7 pc \times 14.7 pc) region to the north-east of Sgr A*, where the soft X-ray emission is notably enhanced. The brightest feature in the field coincides with an extended X-ray source seen in *Chandra* observations which, according to Wang et al. (2002), is a likely PWN. The underlying neutron star may coincide with a *Chandra* point source designated as CXOGCS J174621.5–285256 (Wang et al. 2002), which is located at the peak surface brightness in Fig. 3(c) (i.e. roughly 45 arcsec south of an unrelated point X-ray source which is masked out in this image). The associated nebulosity of the PWN extends up to 1.3 arcmin (3 pc) to the south-east (towards a second unrelated masked source in the *XMM-Newton* image).

This possible PWN, designated G0.13–0.11, has also been described both as an ‘X-ray thread’ and as an ‘X-ray filament’ (e.g. Yusef-Zadeh, Law & Wardle 2002a; Yusef-Zadeh et al. 2002b; Johnson, Dong & Wang 2009).

Excluding the contribution of the PWN, the 2.0–4.5 keV emission in this north-east region must be predominantly thermal in nature as evidenced by the associated S+Ar line flux (Fig. 3d). The peak surface brightness in the S+Ar image coincides with the south-eastern extension of the PWN, suggesting an association between the PWN and the SN which presumably energized the soft-thermal emission. That said, the S+Ar surface brightness remains high over the whole of the central and north-west segment of the image, with a northern extent which can be traced as far as the Quintuplet Star Cluster (the masked source just visible at the top edge of the image).

As noted by a number of authors, the PWN G0.13–0.11 lies in close proximity (at least on the plane of the sky) to the molecular cloud, G0.11–0.11 (also known as the G0.13–0.13 cloud) (Tsuboi, Ukita & Handa 1997; Oka et al. 2001; Yusef-Zadeh et al. 2002a; Handa et al. 2006; Tsuboi et al. 2011). The position of the PWN in relation to the dense molecular gas is illustrated in Fig. 6, which shows both the 4.5–6 keV image and the Fe64 narrow-band image of this region. The bright peak of the PWN (the likely location of the putative pulsar) and the extension to the south-east are very prominent features in the hard 4.5–6 keV band, but are not evident in the line image. Setting aside the PWN emission, there is a strong correlation in Fig. 6 between the 4.5–6 keV and Fe64 data, the former tracing the hard continuum reflected from the dense clouds and latter tracing the iron fluorescence which results from the same X-ray illumination (Park et al. 2004; Koyama et al. 2007a, 2009; Ponti et al. 2010; Capelli et al. 2012). The northern edge of the G0.11–0.11 molecular cloud overlaps with the PWN position, although it remains uncertain whether the PWN is actually embedded in the cloud. An additional link is with the set of narrow non-thermal filaments known as the Radio Arc (Yusef-Zadeh, Morris & Chance 1984), which are aligned at right angles to the Galactic plane and extend over 15 arcmin at $l_{II} \approx 0.18$. A curious aspect of the PWN morphology is a (modest) curvature down its length which matches a bow-shaped radio feature located along the south-western periphery of the Radio Arc region (Wang et al. 2002), suggesting an interaction between the radio filament and the PWN (Wang et al. 2002). It has further been suggested that the collision of the G0.11–0.11 molecular cloud with the enhanced magnetic field of the non-thermal filaments gives rise to the acceleration of particles to relativistic energies; these same particles, once injected, drift along the field lines and hence go on to illuminate the full vertical structure of the filaments (Tsuboi et al. 1997; Yusef-Zadeh et al. 2002a; Tsuboi et al. 2011).

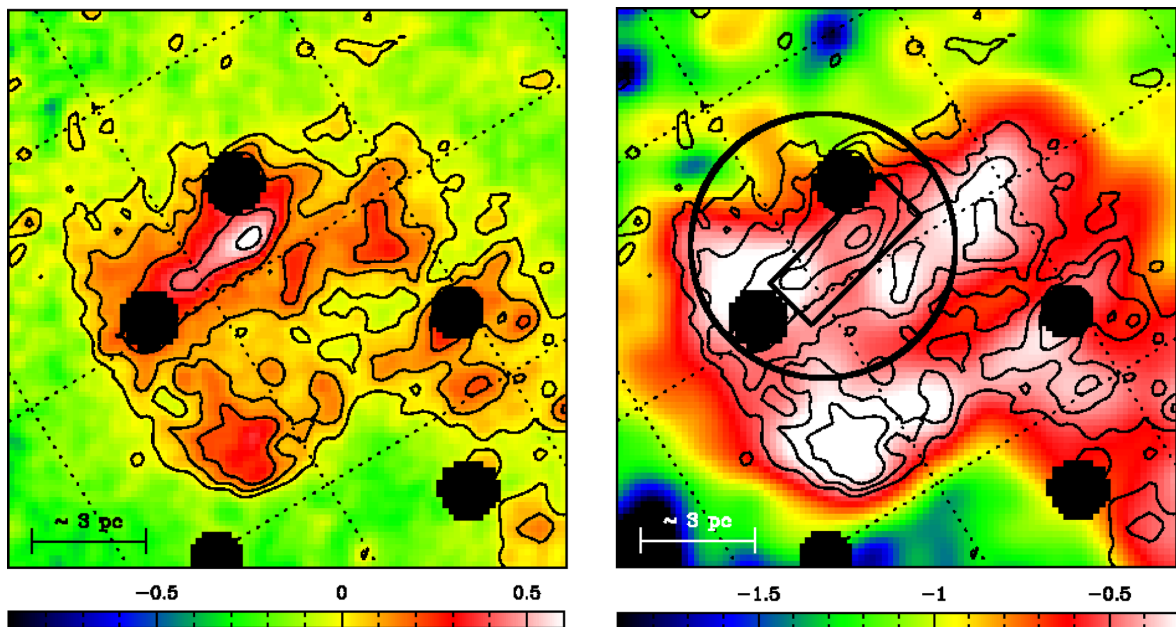


Figure 6. Images of the north-east enhancement covering a 6.3×6.3 arcmin² field. In both cases, the intensity scaling is logarithmic as per the colour bar shown at the bottom of the panel (where the units are \log_{10} (count/20 ks/pixel)). The continuum images have been spatially smoothed using a Gaussian function of width $\sigma = 4$ arcsec, whereas for the Fe64 image $\sigma = 10$ arcsec. The black filled circles correspond to the regions excised by the spatial mask. The dotted lines represent a Galactic coordinate grid with 2.4 arcmin spacing. Left-hand panel: the broad-band 4.5–6 keV image. Right-hand panel: the 6.4-keV line image after subtracting the contribution of the unresolved low-luminosity sources. The black rectangle represents the spectral extraction region used for the PWN G0.13–0.11, whereas the black circle (excluding the rectangular region containing the PWN) defines the spectral extraction region for the surrounding nebulosity. Contours from the 4.5–6 keV image are superimposed.

In the present paper, we focus on the possibility that the region of highest surface brightness in the S+Ar image represents the centre of an SNR. Hereafter, we refer to this source as SNR G0.13–0.12. In order to study the spectral properties of this source, we have extracted spectra from two regions – one encompassing the PWN and the other the brightest region in the S+Ar image (but excluding the PWN at its centre) (see Figs 3d and 6).

5.2 Spectral constraints

The presence of the PWN at the centre of the region in which the soft-thermal emission reaches its peak surface brightness requires special accommodation in the spectral fitting. Our approach was to extract spectra separately from the PWN and SNR regions identified above (noting that the SNR region specifically excludes the PWN region which lies interior to it). The resulting spectra (hereafter referred to as the PWN and SNR spectra) were fitted with a model comprising four emission components, namely the three GC components described earlier (see Section 2.2) plus an absorbed power law representing the continuum emission of the PWN. For the latter the nominal free parameters were the normalization, photon-index Γ and column density N_H ; however in the event we found it necessary to tie the N_H applied to the PWN emission to that pertaining to the soft-thermal emission component. In the spectral fitting, the PWN and SNR spectra were fitted jointly in *XSPEC* with all the parameters, other than the emission component normalizations, tied across the two data sets.

The resulting best-fitting value for the slope of the PWN continuum was $\Gamma = 1.8^{+0.6}_{-0.5}$, fully consistent with the values quoted by Wang et al. (2002) and Johnson et al. (2009). The total 2–10 keV unabsorbed flux of this power-law component was 1.4×10^{-12} erg cm⁻² s⁻¹ (59 percent of which was contained within the PWN

extraction rectangle with the remainder spilling over into the SNR extraction circle). The corresponding X-ray luminosity for a source at the GC distance is 1×10^{34} erg s⁻¹, again broadly consistent with the published estimates.

The best-fitting parameters for the soft-thermal component are listed in the fourth column of Table 2 (where the quoted normalizations and fluxes are the sum across the SNR and PWN regions, thus representing a best estimate of the total flux from the putative SNR). Fig. 5 shows the corresponding best-fitting spectra and residuals for the SNR region. The column density measured for the putative SNR ($5.6^{+0.5}_{-0.4} \times 10^{22}$ cm⁻²) is fully consistent with the fiducial GC N_H referred to earlier. Similarly the temperature of the plasma ($kT = 1.1^{+0.1}_{-0.1}$ keV) is very typical of the GC region (Section 3.2). The inferred abundances relative to solar of Si, S and Ar are all greater than 1, albeit with large errors; however, the weighted average over the three elements is $1.75^{+0.21}_{-0.10}$, indicative of a modest overabundance of these elements in the hot plasma.

Using the best-fitting parameters from Table 2, we have calculated the physical parameters of the X-ray emitting plasma associated with the proposed SNR. In this case the plasma volume was assumed to be spherical and of radius 1.5 arcmin (3.5 pc). The results are summarized in the fourth column of Table 3.

The *VAPEC* thermal plasma model assumes that the plasma is optically thin and in collisional ionization equilibrium (CIE). In order to test the latter assumption, we replaced the *VAPEC* component with a *VNEI* component and re-fitted the model.⁴ The ionization parameter obtained was consistent with $\tau \sim 10^{12}$ cm⁻³ s (with a lower limit of $\sim 7 \times 10^{11}$ cm⁻³ s). For an electron density of

⁴ A Gaussian line had to be included at 3.13 keV to account for the Argon emission which appears not to be included in the *VNEI* code.

$1.2f^{-1/2} \text{ cm}^{-3}$ (Table 3), this implies a lower limit on the ionization time-scale of $1.8 \times 10^4 \text{ yr}$ (assuming $f \sim 1$). In practice, this is consistent with our original assumption of a CIE plasma.

5.3 Comments on the SNR hypothesis

The peak in the X-ray emission for SNR G0.13–0.12 coincides with the southern extension of PWN G0.13–0.11. However, the non-thermal emission from this PWN accounts for only ~ 44 per cent of the total emission. SNR G0.13–0.12 appears to be a centrally concentrated source of thermal X-ray emission consistent with a thermal-composite description.⁵ In thermal-composite SNRs the bright thermal X-ray core is typically accompanied by a shell-like radio morphology, whereas in the present case, there is little concrete evidence for a radio shell or even a partial shell. However, SNR G0.13–0.12 lies within a complex region containing several radio-bright features such as the Radio Arc (Yusef-Zadeh et al. 1984), the Arched filaments (Morris & Yusef-Zadeh 1989) and the Sickle (Lang, Goss & Wood 1997), plus a myriad of fainter structures (e.g. Reich 2003). Hence, the presence of an associated radio shell may, in this instance, be masked. SNR G0.13–0.12 is, in fact, spatially coincident with a structure known as the ‘Bubble’ which is a low-contrast feature in 21 cm radio continuum images (Levine, Morris & Figer 1999), but appears as a prominent cavity in the distribution of warm dust as revealed by 21 μm continuum data (Egan et al. 1998; Price et al. 2001). Simpson et al. (2007) suggest that the source of the dust excitation is likely to be the Quintuplet Cluster, although the cluster is well offset from the centre of the Bubble. In the present context, it is possible to conjecture either that the dust cavity was formed through the interaction of SNR G0.13–0.12 with the surrounding ISM or that SNR G0.13–0.12 exploded into a pre-existing cavity. As noted earlier, in the region of SNR G0.13–0.12, the bright soft X-ray emission extends well beyond the central core and, in particular, can be traced in the north-west sector as far as the Quintuplet Cluster; it is plausible that this is the result of the breakout of the soft-thermal plasma from the SNR into a pre-existing cavity.

From Table 3, the internal thermal energy of SNR G0.13–0.12 is $\sim 3 \times 10^{49} \text{ erg}$ (assuming $f \sim 1$) corresponding to around 3 per cent of the total explosive energy of a SN. Furthermore, the mass contained within the remnant is $\sim 5M_{\odot}$, which is not excessive in the context of the expected ejecta mass from a type II SN explosion (Vink 2012). Therefore, the interpretation of the enhanced soft-thermal emission in this region in terms of a single SN event is credible. The derived plasma temperature ($kT \approx 1.1 \text{ keV}$) is similar to those observed from other thermal-composite SNRs, e.g. IC 443 ($kT \approx 1 \text{ keV}$; Kawasaki et al. 2002), W44 ($kT \approx 0.84 \text{ keV}$; Kawasaki et al. 2005) and Kes 79 ($kT \approx 1.3 \text{ keV}$; Rho & Petre 1998). Earlier we noted from the spectral analysis that the assumption of CIE is valid with an inferred plasma ionization time-scale of at least $1.8 \times 10^4 \text{ yr}$. This is consistent with a thermal-composite classification, since an age of 20 000 yr would seem to be a ubiquitous characteristic of this type of remnant (Vink 2012). Many thermal-composite SNRs show evidence for metal-rich thermal plasmas (see e.g. Lazendic & Slane 2006), which is also in line with our measurement of an overabundance of several alpha elements in the X-ray spectrum of G0.13–0.12.

In thermal-composite remnants the bright thermal X-ray emission may arise when dense cloudlets, which survive the passage of the forward shock from the SN explosion, slowly evaporate and enhance the density of the hot interior (White & Long 1991). In an alternative model, Cox et al. (1999) suggest that as the forward shock decelerates to velocities below $\sim 200 \text{ km s}^{-1}$, strong cooling sets in which diminishes the X-ray emission from the SNR shell. However, the hot thermal X-ray emission from the interior is maintained as the result of thermal conduction (Cui & Cox 1992) and turbulent mixing processes (Shelton et al. 1999).

As mentioned previously, SNR G0.13–0.12 is positioned on the northern boundary of the molecular cloud G0.11–0.11. It has been suggested that an association with molecular clouds may represent a defining characteristic of thermal-composite remnants (Rho & Petre 1998). The presence of dense clouds is in fact a critical ingredient of the cloud-evaporation model (White & Long 1991), that has been successfully applied to thermal-composite remnants such as W28 and 3C 400.2 (Long et al. 1991) and W44 (Rho et al. 1994). If we assume (naïvely) that SNR G0.13–0.12 is in the late Sedov phase, we can determine the density of the medium into which it is expanding as $n \sim (14/R)^5 t^2 E_0$, where n is the density in cm^{-3} , R is the remnant radius in pc, t is its age in units of 10^4 yr and E_0 is the explosion energy in units of 10^{51} erg . Setting $R = 7$ (roughly twice the radius of the centrally bright X-ray emission; see fig. 1 in Rho & Petre 1998), $t = 2$ and $E_0 = 1$, we obtain $n \sim 120 \text{ cm}^{-3}$ suggesting that the progenitor of SNR G0.13–0.12 may have been embedded within a diffuse cloud environment but not within in a dense molecular cloud with $n \sim 10^4 \text{ cm}^{-3}$.

The SNR G0.13–0.12 and the molecular cloud G0.11–0.11 lie within the error box of the EGRET γ -ray source 3EG J1746–2851 (Hartman et al. 1999, see also Yusef-Zadeh et al. 2003). The greatly improved sensitivity and spatial resolution afforded by the *Fermi* LAT has led to the detection of multiple GeV sources in the GC (Abdo et al. 2010a; Nolan et al. 2012) with the source 2FGL J1746.4–2851c positionally coincident with SNR G0.13–0.12 (see also Yusef-Zadeh et al. 2013). A number of other γ -ray sources have been linked with thermal-composite SNRs residing near molecular clouds, including W51C (Abdo et al. 2009), W44 (Abdo et al. 2010b) and IC 443 (Abdo et al. 2010c). The current understanding is that protons and nuclei, accelerated in the SNR shock fronts, subsequently diffuse out of the nebula and interact with nearby molecular material to produce neutral pions (Aharonian, Drury & Voelk 1994), the decay of which gives rise to the γ -ray emission. A VHE counterpart has yet to be unequivocally detected with H.E.S.S. However, the presence of the nearby source, HESS J1745–290, which is thought to be associated with either Sgr A* or PWN G359.95–0.04 (Acero et al. 2010, and references therein), gives rise to significant source confusion in the region of the SNR. However, when the contribution of HESS J1745–290 is subtracted, bright residual TeV emission is evident overlapping the location of SNR G0.13–0.12 and the likely associated molecular cloud (Aharonian et al. 2006).

6 A SUPERBUBBLE IN THE GC?

6.1 Images of the region to the south of Sgr A*

Fig. 3(e) shows the 2–4.5 keV broad-band image of a region to the immediate south of Sgr A* of size $23 \times 21 \text{ arcmin}^2$ ($54 \text{ pc} \times 49 \text{ pc}$). Over much of this field the average surface brightness is less than a third of that pertaining in the north-east region considered earlier. In this southern region, a loop-like structure is apparent which may delineate a potential Galactic superbubble (Mori et al. 2008,

⁵ This class of SNR are also known as mixed-morphology remnants (Rho & Petre 1998; see also Vink 2012).

2009). On the basis of *Suzaku* observations, Mori et al. (2009) define the outer and inner bounds of the loop feature by two ellipses, both centred on $(l_{\text{II}}, b_{\text{II}}) = (+359^{\circ}8312, -0^{\circ}1367)$, with dimensions $20 \times 16 \text{ arcmin}^2$ ($46 \text{ pc} \times 37 \text{ pc}$) and $8 \times 6.4 \text{ arcmin}^2$ ($18.5 \text{ pc} \times 15 \text{ pc}$), respectively. As is evident from Fig. 3(e), the northern part of this structure overlaps the Sgr A East SNR and the south-east lobe of the bipolar outflow, which together provide a very bright backdrop against which it is not possible to discern putative superbubble emission. Outside of this confused region, the loop structure is reasonably complete, although the south-eastern and western segments are particularly well traced by relatively bright emission. The brightest regions apparent in the 2–4.5 keV image correspond to local peaks in the S+Ar line image (Fig. 3f), indicative of the fact that these represent concentrations of hot thermal plasma. Below we investigate the X-ray spectra extracted from the two regions defined by the (small) ellipses in the line image and designated, respectively, as G359.77–0.09 and G359.79–0.26 (see Senda, Murakami & Koyama 2003).

6.2 Spectral constraints

As noted earlier, the G359.79–0.26 region lies outside of the field of view of our standard spectral data set (0202670801) and hence for this source we have been forced to use an alternative observation (0112971001), with a much reduced exposure time.

We utilize the same spectral model as employed previously to study the bipolar outflow (Section 4.2), namely one which accounts for both the underlying emission from unresolved sources and the soft-thermal emission in the region. As usual, we assume initially that the latter can be adequately represented by a single-temperature VAPEC component in XSPEC.

The two-component model provides a good fit to the spectra of both sources. As expected the normalization of the bremsstrahlung component representing the unresolved sources is higher for G359.77–0.09 than G359.79–0.26, commensurate with the location of the former closer to the Galactic plane. The resulting best-fitting parameters pertaining to the soft-thermal plasma emission are reported in the last two columns of Table 2. Fig. 5 shows the corresponding best-fitting spectra and residuals.

The derived temperature for G359.77–0.09 is somewhat lower than that of G359.79–0.26 (approximately 0.7 keV versus 1.0 keV), whereas the N_{H} values show the opposite trend ($5.9 \times 10^{22} \text{ cm}^{-2}$ versus $4.4 \times 10^{22} \text{ cm}^{-2}$). These measurements are in excellent agreement with published results (Mori et al. 2008, 2009). The column-density measurements place the loop structure, unequivocally, within the GC region (Mori et al. 2009). The derived abundances for Si, S and Ar are, in the main, close to solar values and again very consistent with the published results. Interestingly, the hint of a slight overabundance of S and Ar relative to solar in the XMM–Newton data for G359.79–0.26 is also present in the *Suzaku* measurements.

We have again used the best-fitting parameters from Table 2 to determine the physical parameters of the X-ray emitting plasma within G359.77–0.09 and G359.79–0.26. We assumed the plasma to be contained within ellipsoids of dimension $11.1 \text{ pc} \times 5.0 \text{ pc} \times 5.0 \text{ pc}$ and $11.1 \text{ pc} \times 5.5 \text{ pc} \times 5.5 \text{ pc}$, respectively, and then applied the same methodology as discussed earlier. The results are given in the last two columns of Table 3.

Finally, we have tried the experiment of replacing the VAPEC component with the VNEI model in order to test the validity of the assumption that the soft X-ray emitting plasma is in CIE. For both G359.77–0.09 and G359.79–0.26 we found that the inferred ion-

ization parameter, τ , was of the order of $10^{12} \text{ cm}^{-3} \text{ s}$, consistent with our original assumption of CIE. For an electron density in the range $(0.7\text{--}1.1) \text{ cm}^{-3}$ (Table 3), this implies a lower limit on the ionization time-scale ranging from 2.9 to $4.5 \times 10^4 \text{ yr}$ (assuming $f \sim 1$).

6.3 Comments on the superbubble hypothesis

Superbubbles are cavities in the ISM filled with hot plasma, which are formed as a result of sequential co-located SN explosions (Berkhuijsen, Haslam & Salter 1971; Elmegreen & Lada 1977) and/or the combined effect of the stellar winds of an association of OB stars (Castor, McCray & Weaver 1975; Weaver et al. 1977).

Mori et al. (2009) have recently proposed that the enhanced soft X-ray surface brightness within the regions designated as G359.77–0.09 and G359.79–0.26 represent substructure within the extended shell of a superbubble located near to the GC. The argument in favour of this hypothesis revolves around both the morphology of the structure and the fact that the total thermal energy contained within the hot plasma shell is $\sim 10^{51} f^{1/2} \text{ erg}$. Assuming a filling factor f close to unity and that a maximum of 10 per cent of the 10^{51} erg liberated in a SN explosion can be converted to thermal energy (Vink 2012), this implies the need for multiple SN events.

The present results from XMM–Newton confirm that a near-complete X-ray shell can be traced southward of Sgr A* over an extent of roughly 45 pc. The XMM–Newton observations also confirm the thermal nature of this structure and the general properties of the bright sub-regions. The thermal energy contained within the G359.77–0.09 and G359.79–0.26 features are further estimated to be $1.2 \times 10^{50} f^{1/2} \text{ erg}$ and $1.3 \times 10^{50} f^{1/2} \text{ erg}$, respectively. On the basis of these measurements, one can conjecture that these two features might be the result of the passage of the blast wave from separate SN explosions through highly clumped regions of interstellar material (resulting in $f < 1$), and that the shell structure is not a coherent physical entity. However, the apparent limb-brightened characteristics of these two features in relation to the putative loop structure are a persuasive counter-argument.

From the spectral fitting, the ionization time-scales, t_{ion} , for G359.77–0.09 and G359.79–0.26 were estimated to be at least 30 000 yr (assuming $f \approx 1$). For comparison the estimated cooling time-scales listed in Table 3 are two orders of magnitude longer and imply that radiative cooling is not a significant factor. To a rough approximation we may assume that the superbubble structure is in a late Sedov phase of evolution. Taking the radius of the superbubble to be $\sim 20 \text{ pc}$ (the average of the semi-major and semi-minor axes of the outer edge of the shell) and the age to be 30 000 yr, then the Sedov solution gives the density of the medium into which the most recent SN blast wave has expanded to be $\sim 1 \text{ cm}^{-3}$. In the GC context this suggests the presence of a pre-formed cavity, perhaps excavated by earlier SN. However, the same Sedov solution predicts a plasma temperature $\lesssim 0.1 \text{ keV}$, which is at variance with the measured values of 0.7 and 1.1 keV for G359.77–0.09 and G359.79–0.26, respectively. Clearly, in these circumstances a more sophisticated model describing the evolution of a SN explosion within a pre-formed bubble is required (Vink 2012; and references therein). In the present context, it would seem likely that the X-ray bright components represent relatively dense regions within the confines of the superbubble loop structure in which recent shock heating has given rise to an enhanced X-ray luminosity (e.g. Dwarkadas 2005).

The central 100-pc region hosts an array of dense clouds with the potential to leave absorption imprints in soft X-ray images and spectra. The best-studied molecular complex within the bounds of the putative superbubble is the so-called 20 km s⁻¹ cloud, which is a very prominent feature in molecular-line maps (e.g. Oka et al. 1998; Tsuboi et al. 1999; Tsuboi et al. 2011). This cloud is also clearly seen in emission in the *Herschel* 250 μ m image of the GC and, by virtue of its high cold-dust opacity, appears silhouetted against the warmer 70 μ m background in the dust temperature map derived from the *Herschel* data (Molinari et al. 2011). The 20 km s⁻¹ cloud (also known as GCM-0.13–0.08) extends over much of the northern half of the superbubble interior and with a peak molecular hydrogen column density of approximately 6.7×10^{23} cm⁻² (Tsuboi et al. 2011) would certainly shadow any background soft-thermal X-ray emission. In principle, therefore, the apparent deficit of soft X-ray emission from the superbubble interior might be a consequence of a particular pattern in foreground absorption. However, the observed X-ray emission, in particular the morphology of the G359.77–0.09 feature, shows little evidence that it is directly shaped by absorption in the 20 km s⁻¹ cloud [comparing, for example, the SiO $v = 0, J = 2-1$ images in fig. 9 of Tsuboi et al. (2011) with the current X-ray maps]. A ridge-like molecular feature seen in CS $J = 1-0$ images (Tsuboi et al. 1999), in the velocity range -30 – 0 km s⁻¹, similarly runs roughly north–south along the inner edge of the G359.77–0.09 X-ray emission. This molecular feature further extends beyond the southern bound of the superbubble towards the Sgr C region. Soft X-ray absorption arising in this molecular component might explain the gap in the superbubble loop at its southern boundary, but again the evidence for this conjecture is at best tentative.

As previously noted by Mori et al. (2009), the known superbubbles within our own galaxy, typically have very soft X-ray spectra and much larger spatial scales than this GC feature. For example, the Gemini-Monoceros superbubble has a dimension of roughly 140 pc and an X-ray plasma temperature $kT \approx 0.2$ keV (Plucinsky et al. 1996) and the Cygnus superbubble has an extent of roughly 450 pc also with an X-ray plasma temperature $kT \approx 0.2$ keV (Guo et al. 1995). However, recent observations of the Large Magellanic Cloud have led to the discovery of superbubbles with temperatures $kT \sim 1$ keV (e.g. Sasaki et al. 2011; Kavanagh, Sasaki & Points 2012).

A further problem with the GC superbubble interpretation is that there is no known OB association that can be identified as the likely origin of the SN progenitors; however, given the high obscuration towards the GC, current catalogues may be far from complete. There is also a lack of convincing evidence for the loop structure in current radio observations, albeit to the north, the Sgr A radio source provides a bright backdrop against which it would be difficult to trace faint radio emission.⁶

Unfortunately, at present, the evidence supporting the interpretation of the apparent X-ray loop to the south of Sgr A region in terms of a new GC superbubble remains rather inconclusive.

7 SUMMARY AND CONCLUSIONS

In this paper, we have used *XMM-Newton* observations to create a mosaicked X-ray image of the central 100-pc region of the GC in a

variety of bands encompassing both the broad 1–10 keV range and several narrow bands centred on the prominent K-shell lines such as those of helium-like silicon, sulphur, argon and iron. We use these images in combination with X-ray spectral data to investigate the nature of the diffuse soft-thermal X-ray emission pervading the region. From latitudinal cuts through the various images, we find that the bulk of the soft X-ray emission is thermal in nature with a plasma temperature of $kT \approx 1$ keV, subject to absorption by a column density of $N_H \approx 6 \times 10^{22}$ cm⁻². Deviations from this norm are seen in some places, most notably in the region offset between 2 and 10 arcmin to the Galactic south of Sgr A*, where the plasma temperature is enhanced, resulting in the presence of additional helium-like iron line emission over and above that attributable to the unresolved source population studied in Paper I.

Three distinct large-scale features are seen in the 2–4.5 keV image and we investigate the properties of these in some detail. The first is an extended band of emission centred on Sgr A* and aligned perpendicular to the Galactic plane, which is theorized to be a bipolar outflow. We discuss the origin of this bipolar morphology and suggest that the plasma is produced through the shock heating of high-velocity winds emanating from massive stars in the Central Cluster. The resulting outflow may then be collimated by the CND. One problem with this scenario is the sub-structure observed in the feature, which cannot be easily explained if the flow is quasi-continuous. Alternatively, the outflow may be driven by outbursts on Sgr A* as a result of tidal-disruption events occurring at a rate of roughly one event per 4000 yr.

The second feature is the region of enhanced X-ray brightness situated to the north-east of Sgr A*, which is centred on the location of the candidate PWN G0.13–0.11. We suggest that the centrally concentrated thermal X-ray emission represents the core of a thermal-composite SNR. This X-ray source lies (on the plane of the sky) at the edge of the dense molecular cloud G0.11–0.11 and it seems likely that the SNR and molecular cloud have some association. The coincidence of a *Fermi* point source is perhaps indicative of cosmic ray hadrons accelerated in the SNR, interacting with the dense molecular material and via π^0 decay giving rise to the γ -ray emission. This combination of characteristics is commonly observed in thermal-composite SNRs.

Finally, we focus on the extended loop feature to the south of Sgr A*, which has previously been interpreted as the shell of a GC superbubble. Our *XMM-Newton* observations are not inconsistent with this scenario, but unfortunately the evidence in support of this being a coherent physical structure near to the GC remains somewhat tenuous.

ACKNOWLEDGEMENTS

This work is based on *XMM-Newton* observations, an ESA mission with instruments and contributions directly funded by ESA member states and the USA (NASA). VH acknowledges the financial support provided by the UK STFC research council.

REFERENCES

- Abdo A. A. et al., 2009, *ApJ*, 706, L1
- Abdo A. A. et al., 2010a, *ApJS*, 188, 405
- Abdo A. A. et al., 2010b, *Sci*, 327, 1103
- Abdo A. A. et al., 2010c, *ApJ*, 712, 459
- Acero F. et al., 2010, *MNRAS*, 402, 1877
- Aharonian F. A., Drury L. O., Voelk H. J., 1994, *A&A*, 285, 645
- Aharonian F. et al., 2006, *Nat*, 439, 695

⁶ There is a feature in the 90 cm radio data of LaRosa et al. (2000) which extends from the southern boundary of the Sgr A radio complex down towards G359.79–0.26, but any association with the putative superbubble loop looks at best tenuous.

- Alexander T., 2005, *Phys. Rep.*, 419, 65
- Anders E., Grevesse N., 1989, *Geochim. Cosmochim. Acta*, 53, 197
- Arnaud K. A., 1996, in Jacoby G. H., Barnes J., eds, *ASP Conf. Ser. Vol. 101, Astronomical Data Analysis Software and Systems V*, Astron. Soc. Pac., p. 17
- Baganoff F. K. et al., 2003, *ApJ*, 591, 891
- Bélanger G. et al., 2004, *ApJ*, 601, L163
- Berkhuijsen E. M., Haslam C. G. T., Salter C. J., 1971, *A&A*, 14, 252
- Capelli R., Warwick R. S., Porquet D., Gillessen S., Predehl P., 2012, *A&A*, 545, A35
- Castor J., McCray R., Weaver R., 1975, *ApJ*, 200, L107
- Christopher M. H., Scoville N. Z., Stolovy S. R., Yun M. S., 2005, *ApJ*, 622, 346
- Cox D. P., Shelton R. L., Maciejewski W., Smith R. K., Plewa T., Pawl A., Różyczka M., 1999, *ApJ*, 524, 179
- Crocker R. M., Jones D. I., Aharonian F., Law C. J., Melia F., Oka T., Ott J., 2011, *MNRAS*, 413, 763
- Cui W., Cox D. P., 1992, *ApJ*, 401, 206
- Degenaar N., Wijnands R., Cackett E. M., Homan J., in't Zand J. J. M., Kuulkers E., Maccarone T. J., van der Klis M., 2012, *A&A*, 545, A49
- Del Santo M., Sidoli L., Bazzano A., Cocchi M., De Cesare G., Paizis A., Ubertini P., 2006, *A&A*, 456, 1105
- Dwarkadas V. V., 2005, *ApJ*, 630, 892
- Egan M. P., Shipman R. F., Price S. D., Carey S. J., Clark F. O., Cohen M., 1998, *ApJ*, 494, L199
- Elmegreen B. G., Lada C. J., 1977, *ApJ*, 214, 725
- Figer D. F., McLean I. S., Morris M., 1999, *ApJ*, 514, 202
- Figer D. F. et al., 2002, *ApJ*, 581, 258
- Gando Ryu S., Nobukawa M., Nakashima S., Tsuru T. G., Koyama K., Uchiyama H., 2012, preprint (arXiv:1211.4529)
- Genzel R. et al., 2003, *ApJ*, 594, 812
- Ghez A. M. et al., 2008, *ApJ*, 689, 1044
- Gillessen S., Eisenhauer F., Trippe S., Alexander T., Genzel R., Martins F., Ott T., 2009, *ApJ*, 692, 1075
- Guo Z., Burrows D. N., Sanders W. T., Snowden S. L., Penprase B. E., 1995, *ApJ*, 453, 256
- Handa T., Sakano M., Naito S., Hiramatsu M., Tsuboi M., 2006, *ApJ*, 636, 261
- Hartman R. C. et al., 1999, *ApJS*, 123, 79
- Heard V., Warwick R. S., 2013, *MNRAS*, 428, 3462 (Paper I)
- Johnson S. P., Dong H., Wang Q. D., 2009, *MNRAS*, 399, 1429
- Kaneda H., Makishima K., Yamauchi S., Koyama K., Matsuzaki K., Yamasaki N. Y., 1997, *ApJ*, 491, 638
- Kavanagh P. J., Sasaki M., Points S. D., 2012, *A&A*, 547, A19
- Kawasaki M. T., Ozaki M., Nagase F., Masai K., Ishida M., Petre R., 2002, *ApJ*, 572, 897
- Kawasaki M., Ozaki M., Nagase F., Inoue H., Petre R., 2005, *ApJ*, 631, 935
- Koyama K., Awaki H., Kunieda H., Takano S., Tawara Y., 1989, *Nat*, 339, 603
- Koyama K., Maeda Y., Sonobe T., Takeshima T., Tanaka Y., Yamauchi S., 1996, *PASJ*, 48, 249
- Koyama K. et al., 2007a, *PASJ*, 59, 245
- Koyama K., Uchiyama H., Hyodo Y., Matsumoto H., Tsuru T. G., Ozaki M., Maeda Y., Murakami H., 2007b, *PASJ*, 59, 237
- Koyama K., Takikawa Y., Hyodo Y., Inui T., Nobukawa M., Matsumoto H., Tsuru T. G., 2009, *PASJ*, 61, 255
- Lang C. C., Goss W. M., Wood D. O. S., 1997, *ApJ*, 474, 275
- LaRosa T. N., Kassim N. E., Lazio T. J. W., Hyman S. D., 2000, *AJ*, 119, 207
- Launhardt R., Zylka R., Mezger P. G., 2002, *A&A*, 384, 112
- Law C., Yusef-Zadeh F., 2004, *ApJ*, 611, 858
- Lazendic J. S., Slane P. O., 2006, *ApJ*, 647, 350
- Levine D., Morris M., Figer D., 1999, in Cox P., Kessler M., eds, *ESA Special Publication, Vol. 427, The Universe as Seen by ISO*, p. 699
- Long K. S., Blair W. P., Matsui Y., White R. L., 1991, *ApJ*, 373, 567
- Maeda Y. et al., 2002, *ApJ*, 570, 671
- Markoff S., 2010, *Proc. Natl Acad. Sci.*, 107, 7196
- Martins F., Genzel R., Hillier D. J., Eisenhauer F., Paumard T., Gillessen S., Ott T., Trippe S., 2007, *A&A*, 468, 233
- Molinari S. et al., 2011, *ApJ*, 735, L33
- Mori H., Tsuru T. G., Hyodo Y., Koyama K., Senda A., 2008, *PASJ*, 60, 183
- Mori H., Hyodo Y., Tsuru T. G., Nobukawa M., Koyama K., 2009, *PASJ*, 61, 687
- Morris M., Serabyn E., 1996, *ARA&A*, 34, 645
- Morris M., Yusef-Zadeh F., 1989, *ApJ*, 343, 703
- Morris M. et al., 2003, *Astron. Nachr. Suppl.*, 324, 167
- Muno M. P. et al., 2003, *ApJ*, 589, 225
- Muno M. P. et al., 2004, *ApJ*, 613, 326
- Muno M. P., Bauer F. E., Bandyopadhyay R. M., Wang Q. D., 2006, *ApJS*, 165, 173
- Murakami H., Koyama K., Maeda Y., 2001, *ApJ*, 558, 687
- Nobukawa M., Koyama K., Tsuru T. G., Ryu S. G., Tatischeff V., 2010, *PASJ*, 62, 423
- Nobukawa M., Ryu S. G., Tsuru T. G., Koyama K., 2011, *ApJ*, 739, L52
- Nolan P. L. et al., 2012, *ApJS*, 199, 31
- Nord M. E., Lazio T. J. W., Kassim N. E., Hyman S. D., LaRosa T. N., Brogan C. L., Duric N., 2004, *AJ*, 128, 1646
- Oka T., Hasegawa T., Hayashi M., Handa T., Sakamoto S., 1998, *ApJ*, 493, 730
- Oka T., Hasegawa T., Sato F., Tsuboi M., Miyazaki A., 2001, *PASJ*, 53, 779
- Oka T., Nagai M., Kamegai K., Tanaka K., 2011, *ApJ*, 732, 120
- Park S., Muno M. P., Baganoff F. K., Maeda Y., Morris M., Howard C., Bautz M. W., Garmire G. P., 2004, *ApJ*, 603, 548
- Paumard T. et al., 2006, *ApJ*, 643, 1011
- Plucinsky P. P., Snowden S. L., Aschenbach B., Egger R., Edgar R. J., McCammon D., 1996, *ApJ*, 463, 224
- Ponti G., Terrier R., Goldwurm A., Belanger G., Trap G., 2010, *ApJ*, 714, 732
- Porquet D., Rodriguez J., Corbel S., Goldoni P., Warwick R. S., Goldwurm A., Decourchelle A., 2003, *A&A*, 406, 299
- Price S. D., Egan M. P., Carey S. J., Mizuno D. R., Kuchar T. A., 2001, *AJ*, 121, 2819
- Reich W., 2003, *A&A*, 401, 1023
- Revnivtsev M., Sazonov S., Forman W., Churazov E., Sunyaev R., 2011, *MNRAS*, 414, 495
- Rho J., Petre R., 1998, *ApJ*, 503, L167
- Rho J., Petre R., Schlegel E. M., Hester J. J., 1994, *ApJ*, 430, 757
- Rockefeller G., Fryer C. L., Melia F., Warren M. S., 2004, *ApJ*, 604, 662
- Sakano M., Warwick R. S., Decourchelle A., Predehl P., 2004, *MNRAS*, 350, 129
- Sasaki M., Breitschwerdt D., Baumgartner V., Haberl F., 2011, *A&A*, 528, A136
- Schödel R. et al., 2002, *Nat*, 419, 694
- Senda A., Murakami H., Koyama K., 2003, *Astron. Nachr. Suppl.*, 324, 151
- Shelton R. L., Cox D. P., Maciejewski W., Smith R. K., Plewa T., Pawl A., Różyczka M., 1999, *ApJ*, 524, 192
- Sidoli L., Mereghetti S., 1999, *A&A*, 349, L49
- Sidoli L., Mereghetti S., Israel G. L., Chiappetti L., Treves A., Orlandini M., 1999, *ApJ*, 525, 215
- Simpson J. P., Colgan S. W. J., Cotera A. S., Erickson E. F., Hollenbach D. J., Kaufman M. J., Rubin R. H., 2007, *ApJ*, 670, 1115
- Strüder L. et al., 2001, *A&A*, 365, L18
- Tanaka Y., Koyama K., Maeda Y., Sonobe T., 2000, *PASJ*, 52, L25
- Tsuboi M., Ukita N., Handa T., 1997, *ApJ*, 481, 263
- Tsuboi M., Handa T., Ukita N., 1999, *ApJS*, 120, 1
- Tsuboi M., Tadaki K.-I., Miyazaki A., Handa T., 2011, *PASJ*, 63, 763
- Turner M. J. L. et al., 2001, *A&A*, 365, L27
- Vink J., 2012, *A&AR*, 20, 49
- Wang Q. D., Lu F., Lang C. C., 2002, *ApJ*, 581, 1148
- Weaver R., McCray R., Castor J., Shapiro P., Moore R., 1977, *ApJ*, 218, 377
- White R. L., Long K. S., 1991, *ApJ*, 373, 543
- Wijnands R., Miller J. M., Wang Q. D., 2002, *ApJ*, 579, 422
- Yamauchi S., Kawada M., Koyama K., Kunieda H., Tawara Y., 1990, *ApJ*, 365, 532
- Yuasa T., Makishima K., Nakazawa K., 2012, *ApJ*, 753, 129

Yusef-Zadeh F., Morris M., Chance D., 1984, Nat, 310, 557

Yusef-Zadeh F., Law C., Wardle M., 2002a, ApJ, 568, L121

Yusef-Zadeh F., Law C., Wardle M., Wang Q. D., Fruscione A., Lang C. C.,
Cotera A., 2002b, ApJ, 570, 665

Yusef-Zadeh F., Nord M., Wardle M., Law C., Lang C., Lazio T. J. W., 2003,
ApJ, 590, L103

Yusef-Zadeh F., Muno M., Wardle M., Lis D. C., 2007, ApJ, 656, 847

Yusef-Zadeh F. et al., 2013, ApJ, 762, 33

This paper has been typeset from a $\text{\TeX}/\text{\LaTeX}$ file prepared by the author.